Experimental and numerical investigations of octagonal high-strength steel tubular stub columns under combined compression and bending

---

Han Fang[1], Tak-Ming Chan[2,]*, M.ASCE, and Ben Young[3], F.ASCE

Abstract

An experimental and numerical study on the octagonal high-strength steel tubular stub columns under combined compression and bending is presented in this paper. Octagonal high-strength steel tubular stub column specimens with different sizes were prepared. Experiments were performed on these specimens under concentric compression or eccentric compression, which induced various combinations of compression and bending on the structures. In addition, a numerical study through finite-element modelling was also conducted. A finite-element model was developed and validated to be capable of accurately replicating the experimental results. Subsequent parametric studies using the validated model were performed on the structures with a wide range of dimensions and under various combinations of compression and bending. Based on both experimental and parametric studies results, the applicability of existing design approaches in European and American Standards to the structures subject to combined compression and bending was evaluated. The evaluation results show that the design approaches from the standards, especially the compression and bending interaction relationship, provide conservative strength predictions and can be safely applied to the structures.

---

[1] Lecturer, School of Civil, Environmental and Mining Engineering, The University of Adelaide, South Australia 5005, Australia

[2] Associate Professor, Department of Civil and Environmental Engineering, The Hong Kong Polytechnic University, Hong Kong, China

[3] Professor, Department of Civil and Environmental Engineering, The Hong Kong Polytechnic University, Hong Kong, China

*tak-ming.chan@polyu.edu.hk

Keywords

Combined compression and bending; High-strength steel; Local buckling; Octagonal tubes; Stub columns.

Introduction

High-strength steel (HSS) with nominal yield strength above 460MPa has been increasingly applied in the construction industry and used to form structures for buildings, bridges, and long-span structures (Griffis et al. 2003; Uy 2018). Applying HSS allows to reduce the structural element sizes comparing with the structures formed using conventional strength steel. Hence, subsequent benefits including savings of weight consumption of construction materials, easier construction handling, reduction of energy and resources consumption for material manufacture and transportation, and lower environmental impact can be achieved. In order to efficiently design HSS structures with different cross-sectional shapes, material properties and the structural performance of these structures subject to critical loads that may occur to the structures need to be clearly understood. Numerous studies have been performed primarily on the structural performance of HSS structures with I-section and rectangular and circular tubular sections (Rasmussen and Hancock 1995; Shi et al. 2014; Ma et al. 2016; Wang et al. 2016; Somodi and Kövesdi 2017a; Somodi and Kövesdi 2017b; Fang and Chan 2018; Fang and Chan 2019a; Fang and Chan 2019b; Fang et al. 2018a; Wang et al. 2019), among which tubular sections provide relatively higher local buckling resistance (Galambos, 1988). In addition to those tubular cross-section shapes, octagonal tubular structures have also been used in various structural applications (Migita and Fukumoto 1997; Godat et al. 2012; Gonçalves and Camotim 2013). Octagonal tubular cross-sections have been found to have greater local buckling resistance than rectangular tubular cross-sections (Bulson 1969; Naohiro et al. 2017; Zhu et al. 2019) while provide flat surfaces which allow easier connection construction compared with circular tubular cross-sections. Therefore, HSS octagonal tubular structures have become attractive to researchers and manufacturers for their wider applications (Alechnavičius and Bálint 2014; Manoleas et al. 2017). In order to perform safe and accurate design for the structures, the behavior of the structures subject to loading conditions that can occur in practice needs to be clearly characterized.

Existing studies have been performed on octagonal tubular structures formed using both conventional-strength steel and HSS. Experimental investigations have been conducted on octagonal tubular stub columns made of conventional strength steel (Aoki et al. 1991; Migita and Fukumoto 1997; Godat et al. 2012; Zhu et al. 2019). In these studies, residual stresses of octagonal tubular cross-sections with different plate width-to-thickness ratios were characterized and ultimate loads of the stub columns under axial compression were also measured. The ultimate loads obtained from experiments reported in these studies were also compared with those predicted based on Eurocode 3 and ASCE/SEI 48 standards (EN1993-1-1, 2005; ASCE/SEI 48 2011) by Godat et al. (2012) and Zhu et al. (2019) and it has been found that overestimations of the ultimate loads are obtained based on the design approaches in the standards. Apart from the investigations on the structures formed using conventional strength steel, Fang et al. (2018b) investigated the material properties and residual stresses distribution across octagonal HSS tubular cross-sections. The behavior of octagonal HSS tubular stub columns with varying plate width-to-thickness ratios and subject to concentric compression was investigated by Fang et al. (2019) and Chen et al. (2020) through both experimental and numerical investigations. In these studies, unconservative strength predictions for the structures based on Eurocode 3 and ASCE/SEI 48 standards (EN1993-1-1, 2005; ASCE/SEI 48 2011) were also obtained. Accurate design approaches were proposed by Fang et al. (2019). Although effective progress for research studies on the residual stresses and structural behavior of the octagonal tubular stub columns under concentric compression has been obtained in the aforementioned studies, no study on the behavior of the structures under combined loading conditions has been conducted.

Therefore, the behavior of octagonal HSS tubular stub columns under combined compression and bending was investigated in this study. Experiments were firstly conducted on the octagonal HSS tubular stub columns with different sizes and subject to combined compression and bending. A finite-element (FE) model was subsequently developed and validated using the experimental results. The validated FE model was applied to perform extensive parametric studies on the structures with a wide range of dimensions and subject to various combinations of compression and bending. Based on the results from experiments and parametric studies, the applicability of design approaches provided in Eurocode 3, AISC 360 and ASCE/SEI 48 standards to octagonal HSS tubular stub columns under the combined compression and bending was evaluated. The accuracy and reliability of these design approaches were discussed.

Experimental Investigation

General

Octagonal HSS tubular stub column specimens were prepared using S690 HSS plates with nominal yield strength of 690MPa and used for the experimental program to examine the behavior of the structures subject to combined compression and bending. Structures formed using S690 HSS are covered by Eurocode 3 by extending the design approaches for structures made of conventional strength steel to HSS structures with different cross-section shapes. Two cross-sectional sizes selected for the investigations are octagonal hollow sections (OHS) with a nominal plate width (B) of 50 and 70mm respectively and plate thickness of 6mm (OHS-50×6 and OHS-70×6). The specimens with each cross-sectional size were fabricated by cold-bending HSS plates into half-sections and subsequently welding two half-sections to form the specimens. The measurements of material properties, residual stresses, and local geometric imperfections were performed and tests on the octagonal HSS tubular stub column specimens subject to concentric compression or combined compression and bending moment were conducted, as presented in the following sections.

Material properties and residual stresses

Material properties were measured for the octagonal HSS tubular cross-sections through tensile coupon tests. For each cross-sectional size, one flat coupon specimen was extracted from the middle of a flat portion while one cornor coupon was extracted from the corner region, as depicted in Fig. 1. The detailed set-up and procedures for tensile coupon tests have been described by Fang et al. (2018b). The resultant stress-strain curves are presented in Fig. 2 while the measured material properties including elastic modulus (E), 0.2% proof stress ($\sigma_{0.2}$), ultimate tensile strength (σ_u), ultimate tensile strain (ε_u) and the strain at fracture (ε_f) are presented in Table 1. As can be seen in Fig. 2 and Table 1, strength enhancements and reduction of ductility occurred to the corner materials due to the cold-bending fabrication process.

Residual stresses can also exist in the structures due to the cold-bendng and welding fabrication processes; their patterns in octagonal HSS tubular cross-sections with various plate width-to-thickness ratios were characterized using the sectioning method, as presented in Fang et al. (2018b). The results in Fang et al. (2018b) show that both longitudinal membrane and bending residual stresses have been obtained. Based on the measured residual stress distribution and magnitudes across the octagonal HSS tubular cross-sections, a residual stress distribution model was also proposed in the study, as shown in Fig. 3 for a quarter cross-section due to the symmetrical geometry and distribution of cold-bended corners and welding seams for the cross-section. The residual stress distribution obtained using the model was introduced into the FE model in the numerical study, which is described in the later sections.

Tests on stub columns under concentric and eccentric compression

Nine stub column specimens for each cross-sectional size were prepared and tested under concentric or eccentric compression to examine the behaviour of the structures under compression or combined compression and bending respectively. The cross-sectional dimensions and length (L) of the specimens were measured and are presented in Table 1 based on the nomenclature defined in Fig. 1. Initial local geometric imperfections were also measured for the specimens based on the procedures reported in Fang et al. (2019) and the measured imperfection amplitude (ω_0) for each specimen is also provided in Table 1. In the table, the specimens are labeled based on the nominal cross-sectional dimensions and the loading conditions. For example, the specimen "OHS-50×6-e25" represents the stub column specimen with nominal B and thickness (t) of 50 and 6mm, respectively, and tested under eccentric compression based on an nominal initial eccentricity (e) of 25mm. The specimens labeled with "#" represent those specimens for repeated tests. Among the specimens with each cross-sectional size shown in Table 1, two specimens were tested under concentric compression. Seven specimens for each cross-sectional size were tested under eccentric compression, leading to combined compression and bending exerted on each specimen. Prior to testing the stub column specimens, each specimen was milled flat at both ends and each end of a specimen was welded to an end plate of 25mm in thickness.

The tests on the specimens were performed using a 5000kN capacity hydraulic testing machine, as shown in Fig. 4. A pair of knife edges and wedge plates was used to obtain the pin-ended conditions. Slot holes were created on each wedge plate to enable the achievements of varying e values. The initial loading eccentricities were the same at the top and bottom ends to obtain uniform bending moment and various e values were applied in order to generate a range of compressive load-to-bending moment ratios. For the instrumentation during each test, two displacement transducers in front and one displacement transducer at the back were used to measure the end rotations and axial shortening. Another displacement transducer was placed at mid-height of the specimens to obtain the lateral deflection (δ). In addition, four strain gauges were attached to the extreme compressive and tensile fibers of the octagonal HSS tubular cross-sections. The readings from the strain gauges were used to estimate the actual e values of the tests based on the procedures explained by Ma et al. (2019) for nominal e values up to about 50mm. The e values can be calculated as $e = EI\kappa/P - \delta$, where EI is the bending stiffness of the cross-sections, κ is the curvature calculated using the strain gauge readings, and P is the applied compressive load (Ma et al. 2019). For larger e values, the actual e values were measured using a total station based on the space coordinates of both the center of the specimen and that of the knife edge (Ma et al. 2019). The resultant e values are provided in Table 3. During each test, the concentric or eccentric compressive load was applied through displacement control using a rate of 0.3mm/min and paused near the ultimate load for 90s in order to obtain the static ultimate load for each specimen.

The resultant P versus end rotation (θ) curves from the tests for the specimens based on different e values are presented in Figs. 5 and 6 for OHS-50×6 and OHS-70×6 specimens respectively. The ultimate loads ($P_{u,\mathrm{test}}$) and ultimate moment ($M_{u,\mathrm{test}}$) were also obtained for the specimens and are provided in Table 3. Each $M_{u,\mathrm{test}}$ value was estimated as the product of the $P_{u,\mathrm{test}}$ and the sum of calculated e value and corresponding δ measured at $P_{u,\mathrm{test}}$ during each test. Typical local-buckling failure modes obtained for the octagonal HSS tubular stub column specimens are shown in Figs. 7 and 8.

Numerical modeling

General

A numerical study was also performed using the FE analysis package Abaqus in parallel with the experimental investigation described in the previous sections. FE modelling was initially conducted and validated against the test results presented in the previous section. Subsequently, extensive parametric studies were carried out on the octagonal HSS tubular stub columns with different cross-sectional dimensions and subject to varying combinations of compression and bending.

Description of the FE model

The FE model for the structures was developed using four-noded shell elements S4R and taking into account the pin-ended boundary conditions, material properties, initial geometric imperfections and residual stresses for the octagonal HSS tubular stub columns. The shell element with reduced integration was selected because this element type has been successfully applied to accurately predict the structural behavior of a wide range of HSS tubular structures under compression or combined compression and bending (Fang et al. 2018a; Fang et al. 2019; Fang and Chan 2019b; Ma et al. 2019). A mesh size equal to the plate thickness was chosen based on mesh sensitivity studies for the investigations in this study. The material properties used as the input of the FE model were based on the aforementioned measurement results for the flat and corner regions. The stress-strain curves were represented using the stress-strain relationship model provided by Fang et al. (2018b) for the flat and corner regions of octagonal HSS tubular sections and subsequently converted into true stress-log plastic strain curves which were incorporated for the respective regions in the model.

Longitudinal bending and membrane residual stresses have been observed across octagonal HSS tubular cross-sections (Fang et al. 2018b). The effect of bending residual stresses was inherently considered in the input of measured material stress-strain relationship. The property was measured by using the initially curved specimens due to the release of bending residual stresses while extracting the specimens from octagonal HSS tubular cross-sections and subsequently straightening the specimens under loading (Rasmussen and Hancock, 1993; Fang et al. 2019). The magnitudes and pattern of membrane residual stresses were obtained based on the model (Fang et al. 2018b) shown in Fig. 3 and included in the FE model.

The boundary conditions applied in the tests on stub columns under concentric or eccentric compression were replicated in the FE model using two eccentric reference points, which were coupled with the nodes of end surfaces of each stub column specimen. Each reference point was offset with the measured e values in the bending plane of each specimen and located with a longitudinal distance of 112.5mm away from the nearest end surface. At the reference points, the rotation about the axis of buckling was allowed. Besides, the longitudinal translation was also allowed at the reference point on the loaded side. Initial local geometric imperfections can also influence the structural behavior of the octagonal HSS tubular stub columns and were incorporated into the FE model in the form of the lowest elastic eigenmode shape obtained through conducting prior eigenvalue analysis, and with local geometric imperfection amplitudes for the structures (Fang et al. 2019). Two imperfection amplitudes as the measured ω_0 values in Table 1 and the values ($\omega_{\mathrm{D\&W}}$) estimated using the model proposed for octagonal HSS tubular stub columns (Fang et al. 2019), as given by Eq. (1), were used. In the equation, f_{cr} is the elastic buckling stress for the plate with the highest slenderness within a cross-section. Concentric or eccentric loading was applied at the reference point on the loaded side by specifying a displacement in a static Riks step to trace the load-displacement responses of the octagonal HSS tubular stub columns.

$$\omega_{D\&W} = 0.307\left(\sigma_{0.2}/f_{cr}\right)^{0.5} t \qquad (1)$$

FE model validation

The accuracy of the FE model described in the previous section was evaluated by comparing the results from FE modelling with those from tests on the stub column specimens under concentric and eccentric compression. The ultimate loads ($P_{u,\mathrm{FE}}$) and corresponding moments ($M_{u,\mathrm{FE}}$) predicted in FE modelling using different local geometric imperfection amplitudes were first compared with those obtained from the tests, as shown in Table 4. The $P_{u,\mathrm{FE}}$ and $M_{u,\mathrm{FE}}$ values estimated based on the measured ω_0 values compared well with the respective $P_{u,\mathrm{test}}$ and $M_{u,\mathrm{test}}$ values from the stub column tests under concentric and eccentric compression with the mean $P_{u,\mathrm{FE}}/P_{u,\mathrm{test}}$ and $M_{u,\mathrm{FE}}/M_{u,\mathrm{test}}$ ratios of 1.00 and 0.99 and coefficient of variation (COV) of 0.01 and 0.01 respectively. Accurate predictions of $P_{u,\mathrm{FE}}$ and $M_{u,\mathrm{FE}}$ were also obtained based on the $\omega_{\mathrm{D\&W}}$ values and the corresponding mean $P_{u,\mathrm{FE}}/P_{u,\mathrm{test}}$ and $M_{u,\mathrm{FE}}/M_{u,\mathrm{test}}$ ratios are 1.00 and 1.00, with COV of 0.02 and 0.02, respectively. The typical load versus end rotation curves from FE modelling are plotted in Figs. 9 and 10 together with the curves from tests, showing that the load versus end rotation responses were also accurately replicated using the FE model. The local buckling failure modes obtained from the FE modelling also agreed well with those observed during testing the stub column specimens, as shown in Figs. 7 and 8.

Parametric studies

Parametric studies were carried out using the validated FE model on the octagonal HSS stub columns with varying cross-sectional slenderness and under a wide range of combinations of compression and bending. Average material properties measured through the tensile coupon tests were used and the stress-strain curves obtained using the model proposed by Fang et al. (2018b) were converted to the true stress-log plastic strain curves assigned to the respective regions within the octagonal HSS tubular cross-sections. The tubular cross-sections for parametric studies had the B value of 70mm and t values ranging from 4.5 to 10mm. e values for parametric studies were chosen based on the cross-sectional width (*D*) presented in Fig. 1. The *e*/*D* ratios varied between zero and eight for considering a wide range of combined loading. The $\omega_{\mathrm{D\&W}}$ values estimated using Eq. (1) were applied as the initial local geometric imperfection amplitudes based on the arrangements introduced in the previous section. The results from these parametric studies were combined with the stub column test results and the combined results were used for evaluating the applicability of design approaches in standards for the octagonal HSS tubular stub columns under combined compression and bending, as discussed in the following sections.

Design approaches

General

The design approaches given in Eurocode 3 (EN1993-1-1, 2005), AISC 360 (AISC 360, 2016) and ASCE/SEI 48 standards for tubular cross-sections under combined compression and bending were examined for their applicability to octagonal HSS tubular stub columns. The accuracy of these design approaches was evaluated using the results from tests on stub column specimens and parametric studies and discussed in the following sections.

Eurocode 3

Eurocode 3 (EN1993-1-1, 2005) specifies linear interaction relationship between the compressive load and uniaxial bending moment for estimating the cross-sectional resistance under combined compression and bending, as given as Eq. (2). In the equation, P_{d} and M_{d} are the design compressive load and design bending moment respectively. The M_{d} was taken as the end moment based on the *e* values since the octagonal HSS tubular stub columns are relatively short and the amplified second-order moment is only larger than the end moment by 1.5% on average. P_{c} and M_{c} are the resistances of the cross-section under compression and bending moment, respectively. These notations were adopted in this study for the corresponding resistances to obtain the consistency while comparing the interaction relationship for compressive load and uniaxial bending in different standards. P_c can be estimated based on the proposed method in Fang et al (2019). According to the standard, M_c equals the elastic moment capacity (M_{el}) for class 3 cross-sections and is specified as the plastic moment capacity (M_{pl}) for class 1-2 cross-sections. For octagonal HSS tubular cross-section, the cross-section classification in Eurocode 3 has been found to be inaccurate and a modified slenderness limit for class 1-3 cross-sections with elements under compression was proposed (Fang et al. 2019). No specifications for determining class 1-2 octagonal HSS tubular cross-sections under bending have been developed. In the current study, the M_{pl} was used for the octagonal HSS tubular cross-sections with the maximum bending moment larger than the corresponding M_{pl} values when the e/D ratio is eight. The $P_{u,FE}$ under such loading eccentricity was found to be lower than 5% of the P_c in the parametric studies and its effect on the bending moment capacity of the structures would be quite limited.

$$\frac{P_d}{P_c} + \frac{M_d}{M_c} \leq 1 \tag{2}$$

The predicted $P_{d,EC3}$ values are compared with those obtained from parametric studies and tests on the stub column specimens using different initial e values in Fig. 11. Besides, the test and FE results normalised by the P_c and M_{pl} are also plotted in Fig. 12 in comparison with the interactive relationship given in Eurocode 3. It can be observed in the figures that Eurocode 3 provides conservative predictions for octagonal HSS tubular stub columns under combined compression and bending. The mean value of the $P_{u,test+FE}$ over $P_{d,EC3}$ ratios was found to be 1.16 with the COV of 0.10, as provided in Table 5.

AISC 360

The interaction relationship between compression and uniaxial bending is expressed by Eqs. (3) and (4) according to AISC 360 standard (AISC 360, 2016). Because octagonal HSS tubular cross-sections are also not covered in AISC 360 standard, the estimation of P_c and M_c followed the same approach explained in the previous section, allowing the direct comparison of the accuracy of the interaction relationship specified in different standards for cross-section resistance under combined compression and bending. The comparison of predicted $P_{d,AISC}$ values with those obtained from parametric studies and tests on the stub column specimens using different initial e values is also presented in Fig. 11. Besides, the normalised test and FE results using the P_c and M_{pl} are also plotted in Fig. 13 in comparison with the interactive relationship based on AISC 360. As can be seen in the figures, the P_d values were underestimated based on the Eqs. (3) and (4). The mean value of the $P_{u,test+FE}/P_{d,AISC}$ ratios was estimated as 1.09 with the COV of 0.08, as given in Table 5. Comparing with the predictions based on Eurocode 3, the AISC 360 provides more accurate strength predictions.

$$\frac{P_d}{P_c} + \frac{8}{9}\frac{M_d}{M_c} \leq 1 \ for \ \frac{P_d}{P_c} \geq 0.2 \tag{3}$$

$$\frac{P_d}{2P_c} + \frac{M_d}{M_c} \leq 1 \, for \frac{P_d}{P_c} < 0.2 \tag{4}$$

ASCE/SEI 48 standard

Linear interaction relationship expressed by Eq. (2) is also provided in ASCE/SEI 48 standard. Different from Eurocode 3, ASCE/SEI 48 standard specifies that the maximum stress in the cross-sections due to combined compression and bending is the material yield stress. Thus, M_c equals to the M_{el} for the octagonal HSS tubular cross-sections investigated in this study because these cross-sections satisfy the slenderness limit (Fang et al. 2019) and can have their bending moment capacity higher than the M_{el}. The predicted $P_{d,ASCE}$ values are also compared with the $P_{u,test+FE}$ values in Fig. 11 while the normalised test and FE results using the P_c and M_{el} are presented in Fig. 14 in comparison with the interactive relationship based on ASCE/SEI 48. It is clearly shown in the figures that the $P_{d,ASCE}$ predictions are more conservative than those obtained based on Eurocode 3 and AISC 360 standards. The mean value of the $P_{u,test+FE}/P_{d,ASCE}$ ratios was estimated as 1.36 with the COV of 0.14, as shown in Table 5.

Reliability analysis

The reliability of the aforementioned design approaches was evaluated by performing the analysis based on the specifications in EN1990 (EN1990, 2002) and AISC 360 (AISC 360, 2016) standards. For the evaluation, the values provided by Wang et al (2016) for mean-to-nominal yield strength ratio, the COV of material strength and the COV for geometric properties (V_g) were applied. In the reliability analysis for the design method in Eurocode 3 in accordance with EN1990, the key parameters are provided in Table 6 and the definitions of the parameters in the table are: $n_{tests+FE}$ is the number of tests and FE results, $k_{d,n}$ is the design fractile factor, b is the average ratio of test or FE to design model resistance based on a least-squares fit to all the data, V_δ is the COV of tests and FE results relative to the design strengths, V_r is the combined coefficient of variation incorporating both design model and basic variable uncertainties, and γ_{M0} is the required partial safety factor applied to the denominator for predicting the structural strengths. The value estimated to obtain the target reliability index (β) value of 3.8 is 1.02 and larger than the value of 1.0 given in Eurocode 3. Thus, a value of 1.05 for γ_{M0} is recommended to achieve satisfactory reliability of Eurocode 3 for octagonal HSS tubular stub columns under combined compression and bending.

Reliability analysis for the design approach given in AISC 360 and ASCE/SEI 48 was also carried out using the load combination of 1.2×dead load+1.6×live load and a dead-to-live load ratio of 1/3, according to AISC 360. The key parameters are presented in Table 7, where V_Q is the COV of the load effects, V_R is the COV of resistance and ϕ is the safety factor. A value of 0.9 is specified for ϕ in AISC 360 standard and ϕ is applied to the numerator for strength predictions. β values calculated based on the above parameters are 3.28 and 3.60 for AISC 360 and ASCE/SEI 48 respectively, as shown in Table 7. These β values are larger than the required value of 2.6 according to AISC 360, showing that the design approaches in

AISC 360 and ASCE/SEI 48 can be safely applied to the structures subject to combined compression and bending.

Conclusions

Experimental and numerical investigations were performed to examine the behavior of octagonal HSS tubular stub columns subject to combined compression and bending. A total of 18 stub column specimens with different dimensions were prepared. Among these specimens, four of them were tested under concentric compression while fourteen specimens were tested under eccentric compression with varying initial eccentricities to generate different combinations of compression and bending. A FE model was also developed and proven to be capable of replicating the test results on those specimens. Parametric studies using the validated FE model were performed on the octagonal HSS tubular stub columns with a wide range of cross-sectional slenderness and subject to a wide range of combinations of compression and bending.

The results from stub column tests and parametric studies were applied to evaluate the accuracy of design approaches in Eurocode 3, AISC 360 and ASCE/SEI 48 standards based on the interaction relationship between compression and bending. It was found that conservative strength predictions were obtained using these design approaches. Among the design approaches in the standards, the closest predictions were obtained using the approach specified in AISC 360 with the underestimation of 9% on average while the most conservative strength predictions by 36% on average were obtained based on the approach in ASCE/SEI 48 standard. The reliability of these design approaches were also assessed. The design approach in Eurocode 3 with the partial safety factor of 1.05 and the design approaches in AISC 360 and ASCE/SEI 48 standards can be safely applied to octagonal HSS tubular stub columns subject to combined compression and bending.

Data availability statement

Some or all data, models, or codes that support the findings of this study are available from the corresponding author upon reasonable request.

Acknowledgements

The research work presented in this paper was supported by a grant from the Research Grants Council of the Hong Kong Special Administrative Region, China (Project no. PolyU 152189/18E). The authors also appreciate the support from the Chinese National Engineering Research Centre for Steel Construction (Hong Kong Branch) at The Hong Kong Polytechnic University.

References

Alechnavičius, V. and Bálint, J. (2014). “Long span high strength steel trusses.” M. thesis, Luleå Univ. of Tech., Luleå, Sweden.

Aoki, T., Migita, Y. and Fukumoto, Y. (1991). “Local buckling strength of closed polygon folded section columns.” *J. Constr. Steel Res.*, 20, 259-270.

ANSI/AISC 360-16 (2016). “Specification for structural steel buildings.” AISC, Chicago.

ASCE/SEI 48-11 (2011). “Design of steel transmission pole structures.” Reston, Virginia.

Bulson, P.S. (1969). “The strength of thin-walled tubes formed from flat elements.” *Int. J. Mech. Sci.*, 11, 613-620.

Chen, J.B., Zhu, J.Y. and Chan, T.M. (2020). “Experimental and numerical investigation on stub column behaviour of cold-formed octagonal hollow sections.” *Eng. Struct.*, 214, 110669.

EN 1990 (2002). “Eurocode – Basis of structural design.” CEN, Brussels, Belgium.

EN 1993-1-1 (2005). “Eurocode 3: Design of steel structures - Part 1-1: General rules and rules for buildings.” CEN, Brussels, Belgium.

Fang, H. and Chan, T.M. (2018). “Axial compressive strength of welded S460 steel columns at elevated temperatures.” *Thin-Walled Struct.*, 129, 213-224.

Fang, H. and Chan, T.M. (2019a). “Resistance of axially loaded hot-finished S460 and S690 steel square hollow stub columns at elevated temperatures.” *Struct.*, 17, 66-73.

Fang, H. and Chan, T.M. (2019b). “Buckling resistance of welded high-strength-steel box-section members under combined compression and bending.” *J. Constr. Steel Res.*, 162, 105711.

Fang, H., Chan, T.M. and Young, B. (2018a). “Structural performance of cold-formed high strength steel tubular columns.” *Eng. Struct.*, 177, 473-488.

Fang, H., Chan, T.M. and Young, B. (2018b). “Material properties and residual stresses of octagonal high strength steel hollow sections.” *J. Constr. Steel Res.*, 148, 479-490.

Fang, H., Chan, T.M. and Young, B. (2019). “Behavior of octagonal high-strength steel tubular stub columns.” *J. Struct. Eng.*, 145(12), 04019150.

Galambos, T.V. (1988). *Guide to stability design criteria for metal structures*. 4th ed., New York: Wiley.

Griffis, G.L., Axmann, G., Patel, B.V., Waggoner, C.M. and Vinson, J. (2003). “High-strength steel in the long-span retractable roof of reliant stadium.” *NASCC Proc.*, Baltimore, MD, 1-9.

Godat, A., Legeron, F. and Bazonga, D. (2012). “Stability investigation of local buckling behaviour of tubular polygon columns under concentric compression.” *Thin-Walled Struct.*, 53, 131-140.

Gonçalves, R. and Camotim, D. (2013). “Elastic buckling of uniformly compressed thin-walled regular polygonal tubes.” *Thin-Walled Struct.*, 71, 35-45.

Ma, J.L., Chan, T.M. and Young, B. (2016). "Experimental investigation on stub-column behavior of cold-formed high strength steel tubular sections." *J. Struct. Eng.*, 142(5), 04015174-1 to 04015174-11.

Ma, J.L., Chan, T.M. and Young, B. (2019). "Cold-formed high-strength steel rectangular and square hollow sections under combined compression and bending." *J. Struct. Eng.*, 145(12), 04019154.

Manoleas, P., Koltsakis, E. and Veljkovic, M. (2017). "Multiplanar K-joints on cold-formed open sections." *Proc., 8th European Conf. on Steel and Composite Structures*, Copenhagen, Denmark, 629-638.

Migita, Y. and Fukumoto, Y. (1997). "Local buckling behaviour of polygonal sections." *J. Constr. Steel Res.*, 41, 221-233.

Naohiro, W., Kikuo, I., Tadayoshi, O. and Yosuke, K. (2017). "Local buckling behaviour of octagonal hollow cross-section member under axial compression or bending shear." *Proc., 8th European Conf. on Steel and Composite Structures,* Copenhagen, Denmark, 1116-1122.

Rasmussen, K.R. and Hancock, G.J. (1993). "Design of cold-formed stainless steel tubular members. I: Columns." *J. Struct. Eng.*, 119, 2349-2367.

Rasmussen, K.J.R. and Hancock, G.J. (1995). "Tests of high strength steel columns." *J. Constr. Steel Res.*, 34, 27-52.

Shi, G.. Hu, F.X. and Shi, Y.J. (2014). "Recent research advances of high strength steel structures and codification of design specification in China." *Int. J. Steel Struct.*, 14, 873-887.

Somodi, B. and Kövesdi, B. (2017a). "Residual stress measurements on cold-formed HSS hollow section columns." *J. Constr. Steel Res.*, 128, 706-720.

Somodi, B. and Kövesdi, B. (2017b). “Flexural buckling resistance of welded HSS box section members.” *Thin-Walled Struct.*, 119, 266-281.

Uy, B. (2018). “Applications, behavior and construction of high performance steels in steel-concrete composite structures.” *Proc., 12th Int. Conf. on Adv. in Steel-Concrete Composite Structures*, València, Spain, 91-97.

Wang, J., Afshan, S., Gkantou, M., Theofanous, M., Baniotopoulos, C. and Gardner, L. (2016). “Flexural behavior of hot-finished high strength steel square and rectangular hollow sections.” *J. Constr. Steel Res.*, 121, 97-109.

Wang, F.Y., Zhao, O. and Young, B. (2019). “Flexural behaviour and strengths of press-braked S960 ultra-high strength steel channel section beams.” *Eng. Struct.*, 200, 109735.

Zhu, J.Y., Chan, T.M. and Young, B. (2019). “Cross-sectional capacity of octagonal tubular steel stub columns under uniaxial compression.” *Eng. Struct.*, 184, 480-494.

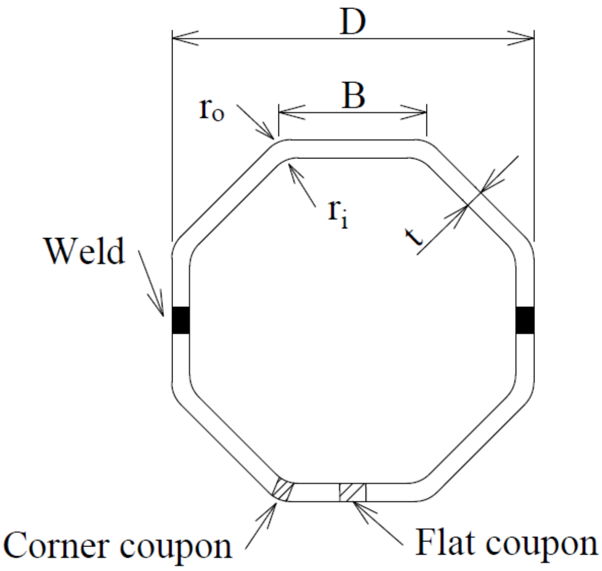

Fig. 1. Octagonal HSS tubular cross-section.

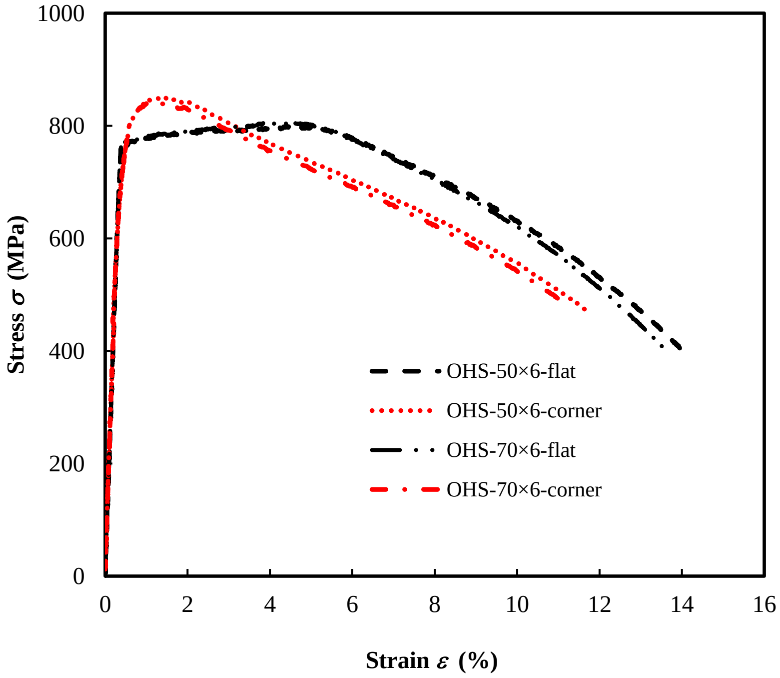

Fig. 2. Measured stress-strain curves for octagonal HSS tubular sections.

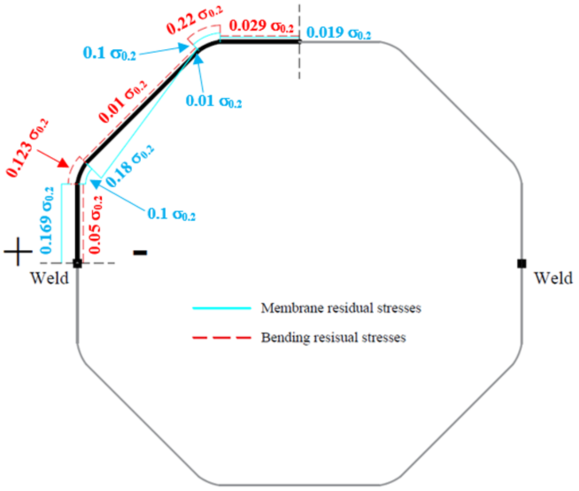

Fig. 3. Residual stress distribution model developed for the octagonal HSS tubular cross-sections in Fang et al. (2018b).

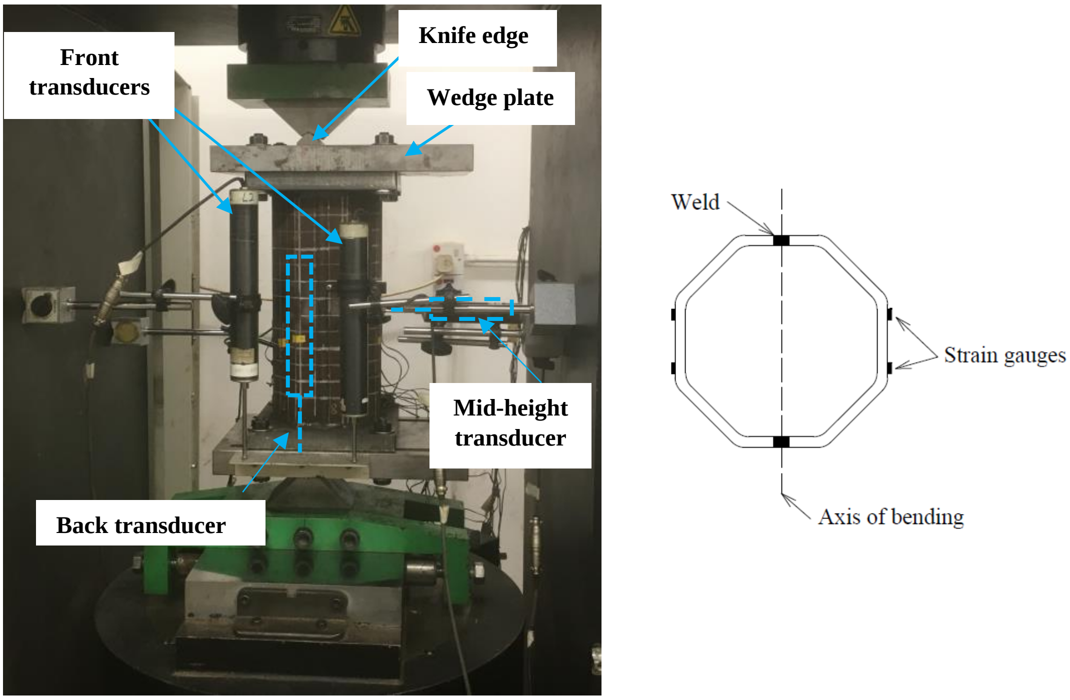

Fig. 4. Test configuration for the specimen under combined compression and bending and strain gauge arrangement.

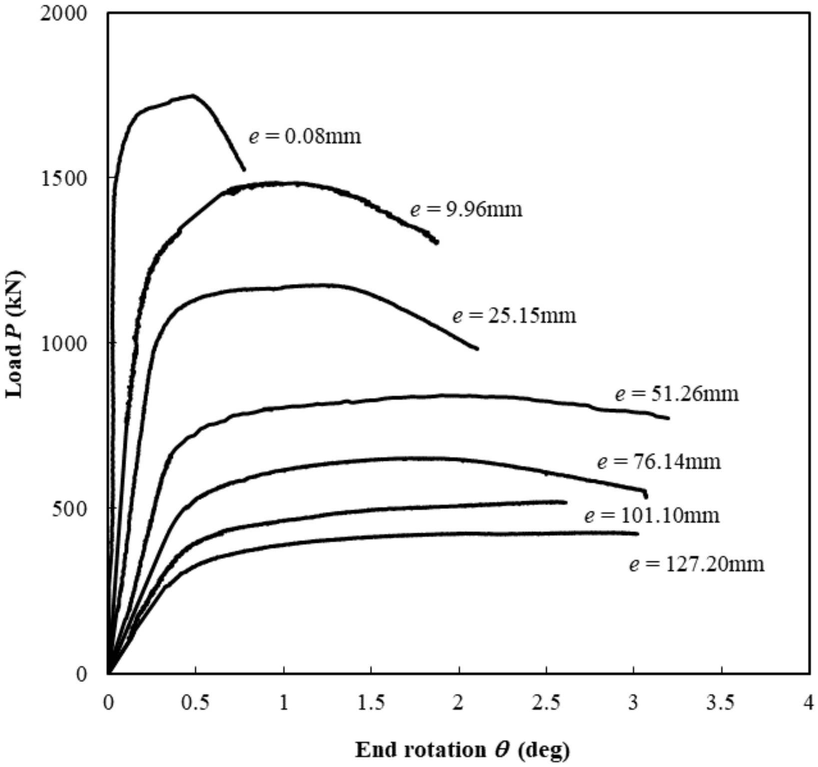

Fig. 5. Load versus end rotation curves for OHS-50×6 stub columns.

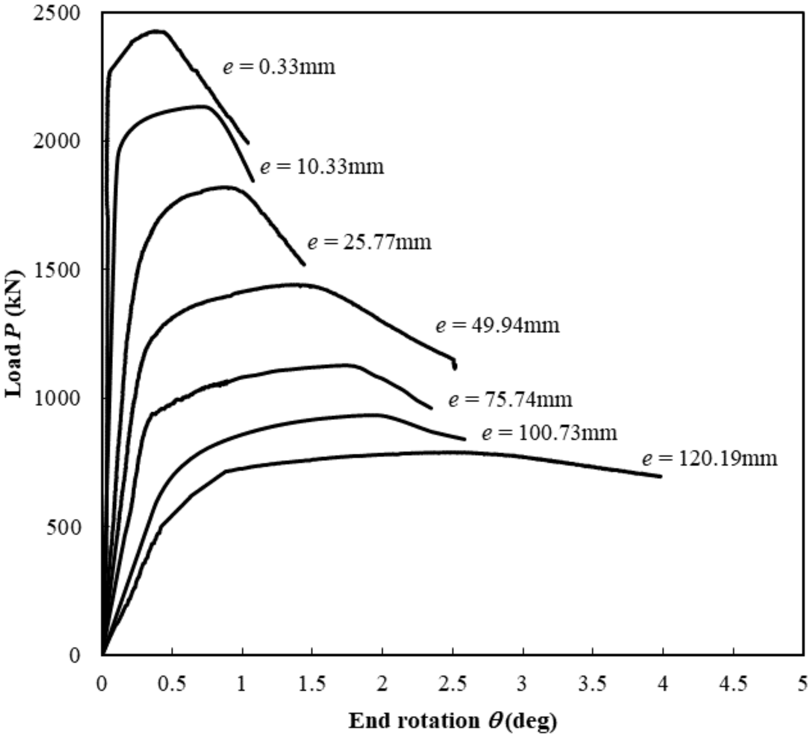

Fig. 6. Load versus end rotation curves for OHS-70×6 stub columns.

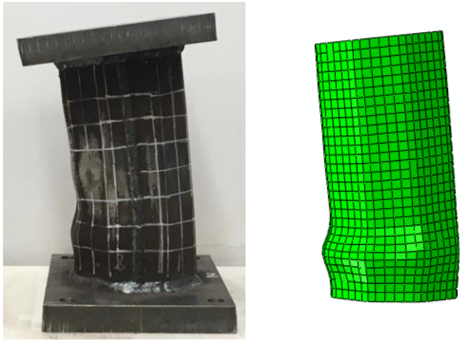

Fig. 7. Failure mode of OHS-50×6-e50 specimen.

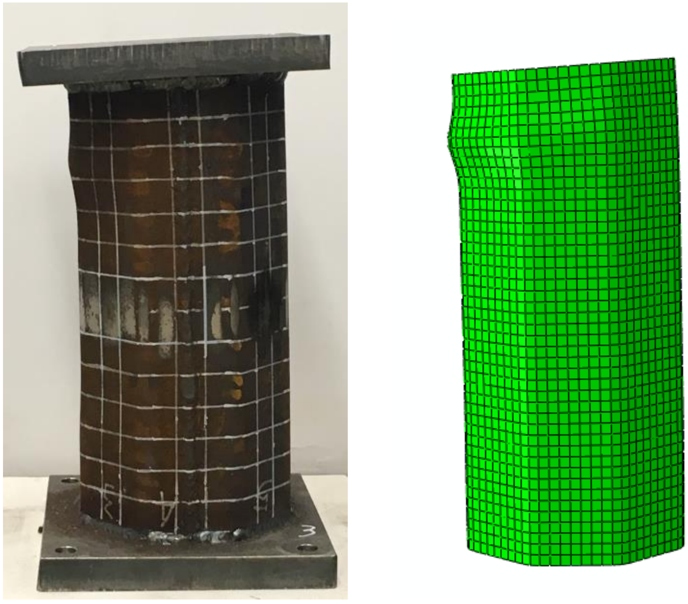

Fig. 8. Failure mode of OHS-70×6-e75 specimen.

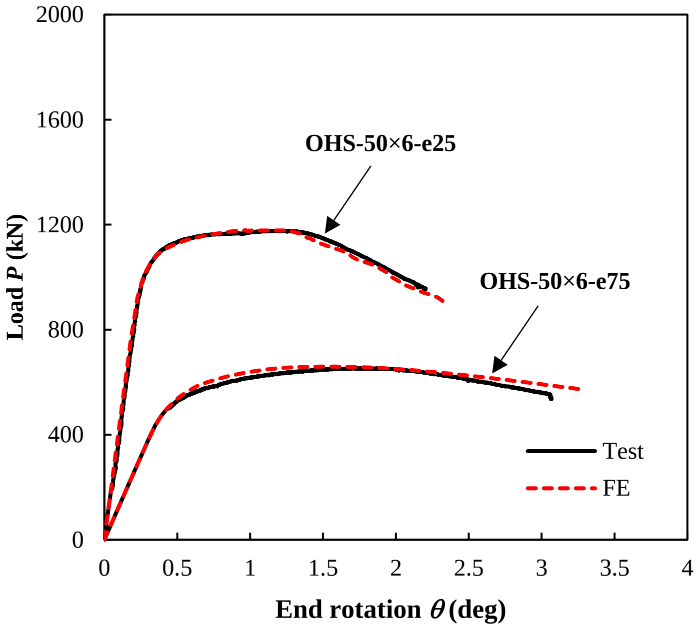

Fig. 9. Comparison of typical load versus end rotation curves predicted in FE modelling for OHS-50 ×6 specimens with those from tests.

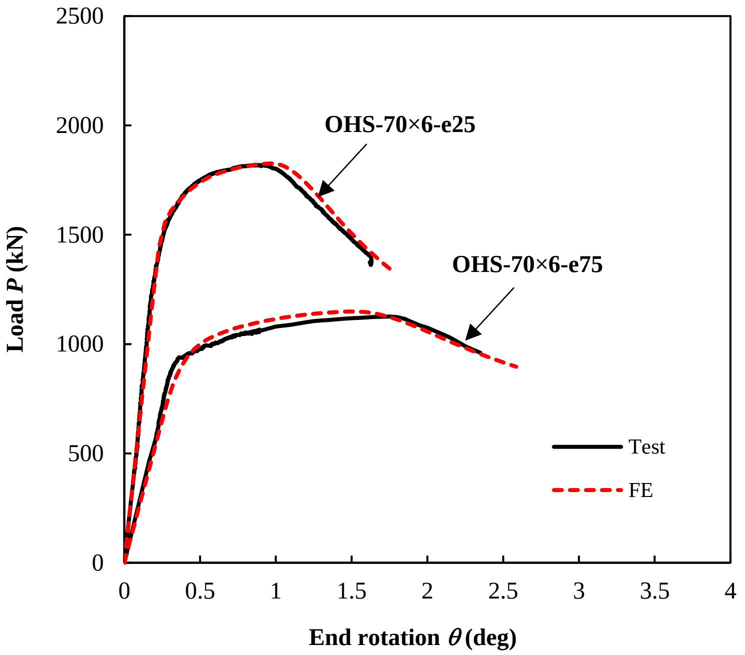

Fig. 10. Comparison of typical load versus end rotation curves predicted in FE modelling for OHS-70 ×6 specimens with those from tests.

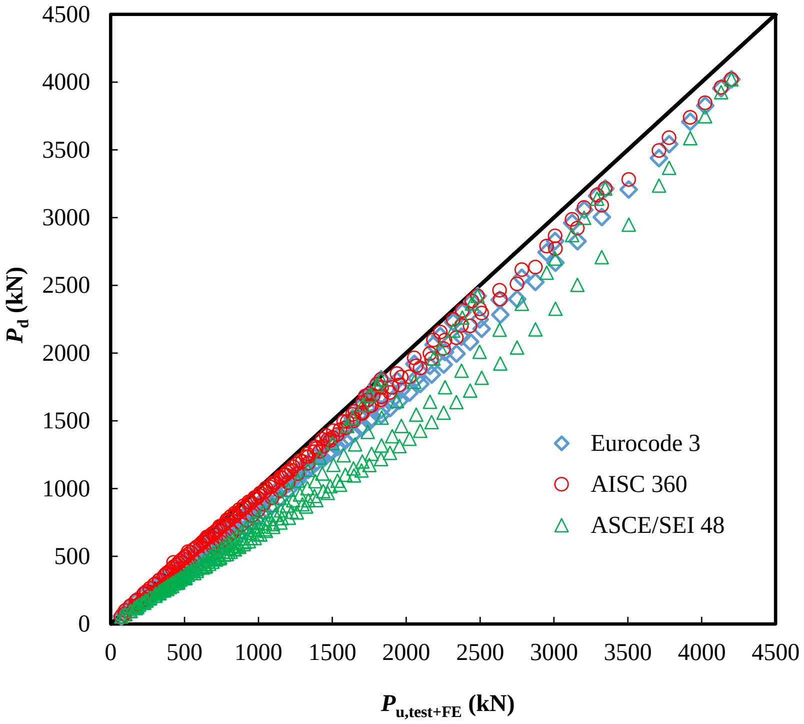

Fig. 11. Comparison of P_d estimated based on different standards with the results from experiments and parametric studies.

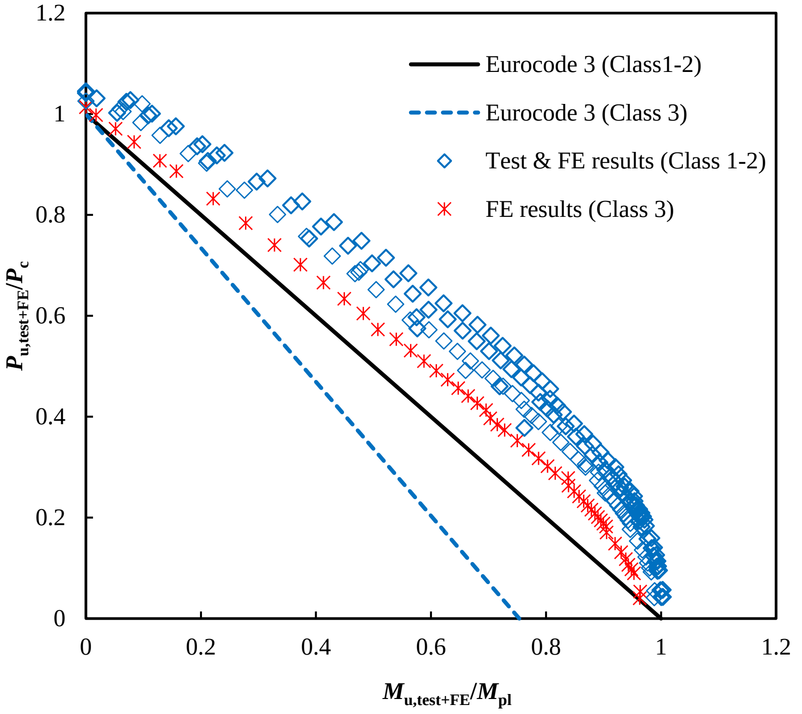

Fig. 12. Comparison of test and FE results normalised by the respective P_c and M_{pl} with the interactive curves from Eurocode 3.

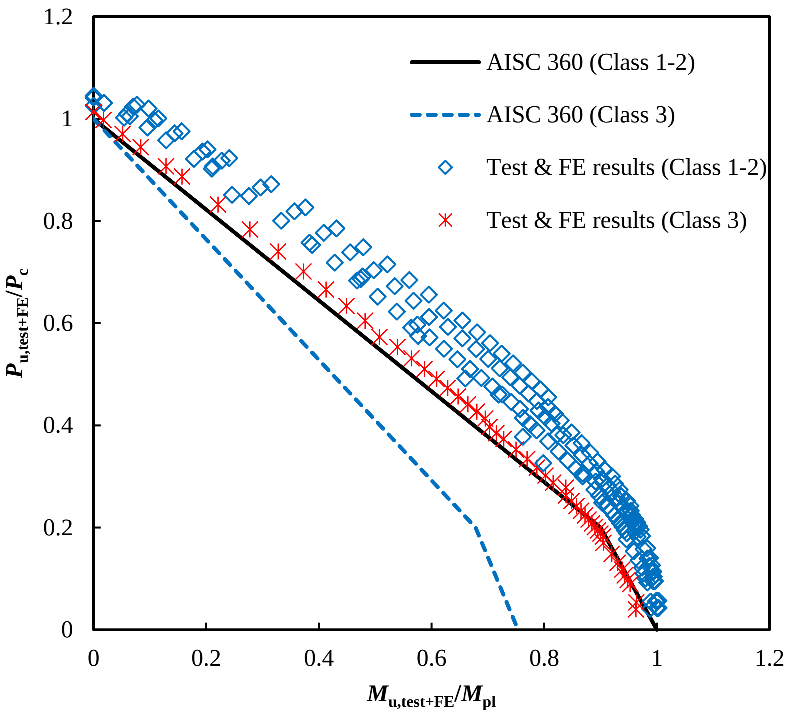

Fig. 13. Comparison of test and FE results normalised by the respective P_c and M_{pl} with the interactive curves from AISC 360.

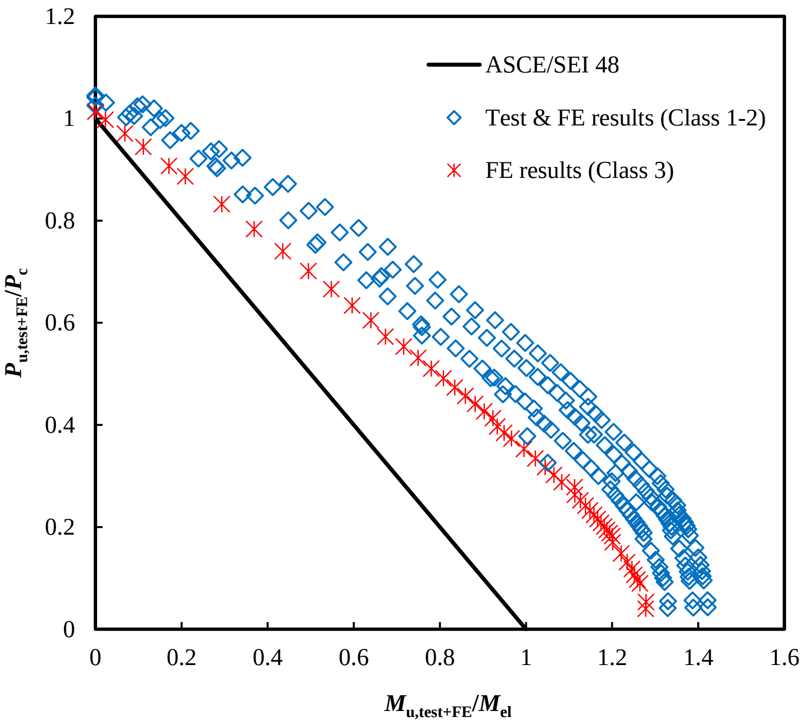

Fig. 14. Comparison of test and FE results normalised by the respective P_c and M_{el} with the interactive curves from ASCE/SEI 48 standard.

Table 1. Measured flat and corner material properties for octagonal HSS tubular sections.

Section	**Cross-sectional region**	***E* (GPa)**	**$\sigma_{0.2}$ (MPa)**	**σ_u (MPa)**	**ε_u (%)**	**ε_f (%)**
OHS-50×6	Flat	213	756	800	4.6	13.6
	Corner	199	780	850	1.3	11.9
OHS-70×6	Flat	215	760	801	4.4	14.0
	Corner	196	785	840	1.2	11.3

Table 2. Dimensions of octagonal HSS tubular stub column specimens.

Section	**Edge length *B* (mm)**	**Thickness *t* (mm)**	**Outer corner radius r_o (mm)**	**Inner corner radius r_i (mm)**	**Length *L* (mm)**	**ω_0 (mm)**
OHS-50×6-e0	50.1	5.89	20.0	14.0	232.0	0.49
OHS-50×6-e0#	50.3	5.95	20.0	14.0	231.3	0.55
OHS-50×6-e10	49.6	5.92	20.0	14.0	230.3	0.58
OHS-50×6-e25	49.7	5.95	20.0	14.0	230.0	0.40
OHS-50×6-e25#	49.5	5.89	19.5	15.5	231.0	0.46
OHS-50×6-e50	48.9	5.90	20.0	14.0	230.7	0.56
OHS-50×6-e75	50.1	5.90	20.0	14.0	230.7	0.52
OHS-50×6-e100	49.7	5.90	20.0	14.0	229.5	0.60
OHS-50×6-e125	49.6	5.89	20.0	14.0	229.2	0.64
OHS-70×6-e0	69.5	5.88	20.0	14.0	358.0	0.71
OHS-70×6-e0#	69.1	6.01	21.0	15.0	359.5	0.65
OHS-70×6-e10	66.8	5.92	21.0	15.0	357.5	0.64
OHS-70×6-e25	70.1	6.00	20.0	14.0	358.6	0.70
OHS-70×6-e50	70.4	5.90	20.0	14.0	359.3	0.59
OHS-70×6-e50#	69.3	6.02	20.0	14.0	357.6	0.63
OHS-70×6-e75	69.4	5.84	20.0	14.0	358.3	0.68
OHS-70×6-e100	68.6	5.92	21.0	15.0	359.7	0.74
OHS-70×6-e120	69.5	5.92	20.0	14.0	351.9	0.73

Note: # = repeated tests.

Table 3. Results of stub column tests under concentric or eccentric compression.

Section	***e (mm)***	**$P_{u,\text{test}}$ (kN)**	**$M_{u,\text{test}}$ (kNm)**
OHS-50×6-e0	0.08	1723.5	4.5
OHS-50×6-e0#	-0.04	1778.5	6.8
OHS-50×6-e10	9.96	1460.3	17.1
OHS-50×6-e25	25.15	1177.1	33.0
OHS-50×6-e25#	24.86	1185.6	33.2
OHS-50×6-e50	51.26	843.2	45.9

OHS-50×6-e75	76.14	653.1	57.2
OHS-50×6-e100	101.10	524.4	60.4
OHS-50×6-e125	127.20	426.3	62.8
OHS-70×6-e0	0.33	2420.5	7.3
OHS-70×6-e0[#]	0.03	2490.0	2.5
OHS-70×6-e10	10.33	2189.7	28.6
OHS-70×6-e25	25.77	1818.3	52.4
OHS-70×6-e50	49.94	1441.7	77.6
OHS-70×6-e50[#]	51.61	1388.6	77.8
OHS-70×6-e75	75.74	1111.2	97.1
OHS-70×6-e100	100.73	912.7	102.9
OHS-70×6-e120	120.19	787.4	107.8

Note: # = repeated tests.

Table 4. Comparison of test results with FE results based on different imperfection amplitudes

Section	**Measured amplitude ϖ_0**		**Calculated $\varpi_{D\&W}$ (Eq. (1))**	
	$P_{u,FE}/P_{u,test}$	$M_{u,FE}/M_{u,test}$	$P_{u,FE}/P_{u,test}$	$M_{u,FE}/M_{u,test}$
OHS-50×6-e0	1.00	1.00	1.00	1.00
OHS-50×6-e0[#]	0.99	0.98	1.01	1.00
OHS-50×6-e10	0.98	0.98	0.99	0.99
OHS-50×6-e25	1.01	1.02	0.98	0.98
OHS-50×6-e25[#]	0.99	0.98	0.98	0.97
OHS-50×6-e50	1.01	1.01	1.02	1.02
OHS-50×6-e75	0.99	0.98	0.98	0.98
OHS-50×6-e100	1.00	1.00	1.02	1.02
OHS-50×6-e125	1.02	1.00	1.03	1.02
OHS-70×6-e0	1.00	0.99	1.01	0.99
OHS-70×6-e0[#]	1.00	1.00	1.00	1.00
OHS-70×6-e10	0.98	0.98	0.98	0.98
OHS-70×6-e25	1.00	1.00	1.00	1.01
OHS-70×6-e50	1.01	1.02	0.99	1.00
OHS-70×6-e50[#]	1.00	1.00	1.01	1.01
OHS-70×6-e75	0.99	0.99	0.99	0.99
OHS-70×6-e100	0.99	0.99	1.01	1.01
OHS-70×6-e120	1.01	1.01	1.03	1.03
Mean	1.00	0.99	1.00	1.00
COV	0.01	0.01	0.02	0.02

Note: # = repeated tests.

Table 5. Comparison of test and parametric studies results with the predicted strengths based on different standards

$n_{tests+FE}$	**Parameters**	$P_{u,\mathrm{test+FE}}/P_{d,\mathrm{EC}}$	$P_{u,\mathrm{test+FE}}/P_{d,\mathrm{AISC}}$	$P_{u,\mathrm{test+FE}}/P_{d,\mathrm{ASCE}}$
222	Mean	1.16	1.09	1.36
	COV	0.10	0.08	0.14

Table 6. Statistical parameters for the Eurocode 3 reliability analysis

$n_{tests+FE}$	$k_{d,\mathrm{n}}$	b	V_δ	V_r	γ_{M0}
222	3.135	1.16	0.09	0.102	1.02

Table 7. Statistical parameters for the reliability analysis according to AISC 360.

Standard	$n_{tests+FE}$	V_Q	V_R	ϕ	β
AISC360	222	0.19	0.11	0.9	3.28
ASCE/SEI48	222	0.19	0.16	0.9	3.60